J. Fluid Mech. (2016), *vol.* 799, *pp.* 413–432. © Cambridge University Press 2016
doi:10.1017/jfm.2016.394

Transition to geostrophic convection: the role of the boundary conditions

Rudie P. J. Kunnen[1,†], Rodolfo Ostilla-Mónico[2], Erwin P. van der Poel[2], Roberto Verzicco[3,2] and Detlef Lohse[2]

[1]Fluid Dynamics Laboratory, Department of Applied Physics, and J. M. Burgers Centre for Fluid Dynamics, Eindhoven University of Technology, P.O. Box 513, 5600 MB Eindhoven, The Netherlands

[2]Physics of Fluids Group, Mesa+ Institute, and J. M. Burgers Centre for Fluid Dynamics, University of Twente, P.O. Box 217, 7500 AE Enschede, The Netherlands

[3]Dipartimento di Ingegneria Industriale, University of Rome 'Tor Vergata', Via del Politecnico 1, Roma 00133, Italy

(Received 15 December 2015; revised 18 April 2016; accepted 5 June 2016; first published online 23 June 2016)

Rotating Rayleigh–Bénard convection, the flow in a rotating fluid layer heated from below and cooled from above, is used to analyse the transition to the geostrophic regime of thermal convection. In the geostrophic regime, which is of direct relevance to most geo- and astrophysical flows, the system is strongly rotating while maintaining a sufficiently large thermal driving to generate turbulence. We directly simulate the Navier–Stokes equations for two values of the thermal forcing, i.e. $Ra = 10^{10}$ and $Ra = 5 \times 10^{10}$, at constant Prandtl number $Pr = 1$, and vary the Ekman number in the range $Ek = 1.3 \times 10^{-7}$ to $Ek = 2 \times 10^{-6}$, which satisfies both requirements of supercriticality and strong rotation. We focus on the differences between the application of no-slip versus stress-free boundary conditions on the horizontal plates. The transition is found at roughly the same parameter values for both boundary conditions, i.e. at $Ek \approx 9 \times 10^{-7}$ for $Ra = 1 \times 10^{10}$ and at $Ek \approx 3 \times 10^{-7}$ for $Ra = 5 \times 10^{10}$. However, the transition is gradual and it does not exactly coincide in Ek for different flow indicators. In particular, we report the characteristics of the transitions in the heat-transfer scaling laws, the boundary-layer thicknesses, the bulk/boundary-layer distribution of dissipations and the mean temperature gradient in the bulk. The flow phenomenology in the geostrophic regime evolves differently for no-slip and stress-free plates. For stress-free conditions, the formation of a large-scale barotropic vortex with associated inverse energy cascade is apparent. For no-slip plates, a turbulent state without large-scale coherent structures is found; the absence of large-scale structure formation is reflected in the energy transfer in the sense that the inverse cascade, present for stress-free boundary conditions, vanishes.

Key words: rotating turbulence, turbulent convection, turbulent flows

† Email address for correspondence: r.p.j.kunnen@tue.nl

1. Introduction

Natural convection is ubiquitous in Nature. It is found not only in the Earth's interior and oceans, but also in planetary atmospheres and inside stars (Marshall & Schott 1999; Miesch 2000; Roberts & Glatzmaier 2000; Heimpel, Aurnou & Wicht 2005). In all of those flows, the background rotation induces a Coriolis force, which significantly affects the system, changing not only the flow phenomenology but in many cases also the heat transport and the amount of mixing of different species.

Rotating Rayleigh–Bénard (RB) convection, the flow between two rotating parallel plates heated from below and cooled from above, is commonly used as a model for studying rotating thermal convection. Rotating an RB system induces many changes. First, as found experimentally by Nakagawa & Frenzen (1955) and demonstrated using linear stability analysis by Chandrasekhar (1961), convective instability sets in at increasingly higher temperature differences when rotation is applied, or, in other words, the critical value of the Rayleigh number (the non-dimensionless temperature difference between the plates) rises as a function of the non-dimensional rotation rate, i.e. the inverse Ekman number. In experiments (Rossby 1969; Zhong, Ecke & Steinberg 1993; Liu & Ecke 1997, 2009; King *et al.* 2009; Zhong *et al.* 2009; Weiss *et al.* 2010; Zhong & Ahlers 2010; Kunnen *et al.* 2011; Weiss & Ahlers 2011*a*,*b*; Ecke & Niemela 2014; Stellmach *et al.* 2014; Cheng *et al.* 2015) and numerical simulations (Kunnen, Clercx & Geurts 2006, 2008*a*; King *et al.* 2009; Zhong *et al.* 2009; Schmitz & Tilgner 2009, 2010; Stevens, Clercx & Lohse 2010; Weiss *et al.* 2010; Horn & Shishkina 2014; Stellmach *et al.* 2014; Cheng *et al.* 2015), when considering the dependence on rotation of the convective heat flux through the fluid layer, one can typically distinguish different regimes: (i) rotation is too weak to significantly alter the heat flux ('rotation-unaffected'); (ii) rotation plays a role, and depending on the Prandtl number of the fluid, the heat flux may rise or fall with increasing rotation ('rotation-affected'); and (iii) rotation is dominant, the principal force balance is the geostrophic balance (Greenspan 1968), and the heat transfer is rapidly reduced as rotation increases ('rotation-dominated' or geostrophic regime). Based on estimates of the governing parameters for geophysical and astrophysical flow settings, these flows are expected to fall in the geostrophic regime of convection. By studying this regime, we aim to extend understanding of the aforementioned large-scale flows.

King *et al.* (2009) performed the first comprehensive investigation into the transition between the rotation-affected and rotation-dominated (geostrophic) regimes. They argued, based on a large dataset of experimental and numerical results, that the transition happens when the kinetic boundary layer (of Ekman type; Greenspan 1968) becomes smaller than the thermal boundary layer. Using numerical simulations with stress-free plates instead of the usual no-slip walls, they actually found a similar transition in the local scaling laws, however with different prefactors (King *et al.* 2009, supplement). This transition was later confirmed by the simulations of Schmitz & Tilgner (2009, 2010).

Julien and coworkers took a different approach in order to be sure to study the geostrophic regime. In a series of articles (Sprague *et al.* 2006; Julien *et al.* 2012*a*,*b*; Rubio *et al.* 2014), they derived a set of reduced equations representative of the limit of strong rotation (i.e. vanishing Rossby number) and described many properties of geostrophic convection. In particular, they identified different flow states. Just above onset, convection sets in with a cellular structure (also see e.g. Nakagawa & Frenzen 1955; Chandrasekhar 1961). Once the thermal forcing is increased, the flow becomes organised into columnar vortices covering the entire

vertical extent of the domain, which are also referred to as convective Taylor columns (Sakai 1997; Sprague *et al.* 2006; Portegies *et al.* 2008; King *et al.* 2009; Grooms *et al.* 2010; Kunnen, Clercx & Geurts 2010*a*; King & Aurnou 2012). A remarkable characteristic feature of these structures is the sleeve of oppositely signed vorticity surrounding the vortical core. At even higher thermal forcing, the columns lose their vertical coherence. Instead, swirling plumes erupt vertically from the bottom and top boundary layers and do not cross the fluid layer entirely (Rossby 1969; Zhong *et al.* 1993; Julien *et al.* 1996; Kunnen *et al.* 2006; King *et al.* 2009; Zhong *et al.* 2009; Kunnen *et al.* 2010*a*). At the strongest thermal forcing, another state was observed, coined 'geostrophic turbulence', in which vertical coherence has vanished completely and a fluctuating field remains. Note that these four different flow states are all part of the rotation-dominated geostrophic regime. These flow structures have been reproduced in direct numerical simulations (DNS) of the full Navier–Stokes equations (Stellmach *et al.* 2014) and laboratory visualisations (Cheng *et al.* 2015). An intriguing feature of the geostrophic-turbulence state is the formation of an inverse energy cascade (Rubio *et al.* 2014). In an inverse cascade, unlike the regular cascade of three-dimensional (3D) homogeneous isotropic turbulence, energy flows from the small length scales to larger ones. This leads to the formation of large-scale structures (the depth-independent barotropic mode (Rubio *et al.* 2014)) that typically become comparable in size to the domain in which they reside. Such self-organisation and the inverse cascade have also been reported in recent DNS employing stress-free boundaries (Favier, Silvers & Proctor 2014; Guervilly, Hughes & Jones 2014; Stellmach *et al.* 2014).

The difficulty of achieving the geostrophic regime is twofold. Both a high rotation rate and a significant level of thermal driving, to remain turbulent even with respect to the increased critical Rayleigh number, are needed to achieve the geostrophic regime. Most earlier experimental and numerical studies of rotating RB flow (Rossby 1969; Zhong *et al.* 1993; Julien *et al.* 1996; Liu & Ecke 1997; Vorobieff & Ecke 2002; Kunnen *et al.* 2008*a*; Kunnen, Clercx & Geurts 2008*b*; King *et al.* 2009; Liu & Ecke 2009; Zhong *et al.* 2009; Schmitz & Tilgner 2009, 2010; Kunnen, Geurts & Clercx 2010*b*; Stevens *et al.* 2010; Weiss *et al.* 2010; Zhong & Ahlers 2010; Kunnen *et al.* 2011; Liu & Ecke 2011; Weiss & Ahlers 2011*a*,*b*; Stevens, Clercx & Lohse 2012; Kunnen, Corre & Clercx 2013; Horn & Shishkina 2014) – and see Stevens, Clercx & Lohse (2013*a*) for a recent review – have not conclusively ventured deep into the geostrophic regime, so that any scaling ranges in the geostrophic regime are rather narrow. Recent experiments (Ecke & Niemela 2014; Cheng *et al.* 2015) and DNS (Stellmach *et al.* 2014), capable of simultaneously achieving very high Rayleigh numbers $Ra \gtrsim 10^9$ and very low Ekman numbers $Ek \lesssim 10^{-6}$, have found the transitions in the scaling laws for the heat transfer reported previously over a wider parameter range and could achieve wider scaling ranges in the geostrophic regime.

The geostrophic regime is a natural extension of the weakly nonlinear theories developed for rotating convection near onset (Veronis 1968; Clune & Knobloch 1993; Bassom & Zhang 1994; Dawes 2001; Ecke 2015). A remarkable prediction of the theory is that, for strong enough rotation, the flow becomes independent of the boundary conditions (no-slip or stress-free; Niiler & Bisshopp 1965; Heard & Veronis 1971; Clune & Knobloch 1993; Dawes 2001). This result has been challenged recently (Stellmach *et al.* 2014, and the current work). In terms of heat transfer, the weakly nonlinear theory (Bassom & Zhang 1994; Dawes 2001) predicts a dependence $Nu = 2\epsilon$ of the Nusselt number Nu (dimensionless convective heat transfer) on the normalised distance from onset, $\epsilon = Ra/Ra_c - 1$, where Ra_c is the critical Rayleigh number. This prediction matches nicely with the results near onset from the asymptotic

equations (Julien *et al.* 2012*a*) and, by extension, of the stress-free DNS (Stellmach *et al.* 2014). Ecke (2015) argues that also the no-slip DNS results of Stellmach *et al.* (2014) are consistent with weakly nonlinear theory.

However, a complete picture of what is happening during the transition to the geostrophic regime, and where it takes place in the parameter space, is still missing. In this paper we present numerical simulations covering the transition to geostrophic convective turbulence using the full Navier–Stokes equations for a single Prandtl number. We analyse in detail the effects of the choice of boundary conditions, i.e. including or omitting the Ekman layers. In § 2 we describe the numerical method and give the parameter values for the runs. The results for the convective heat transfer are presented in § 3. In § 4 we consider the effects of rotation on the boundary-layer scales and on the volumetric distribution of kinetic energy and thermal variance dissipation, an approach that has allowed for the Grossmann–Lohse theory of heat transfer in non-rotating RB flow (Grossmann & Lohse 2000, 2001, 2004; Stevens *et al.* 2013*b*). The flow phenomenology and its relation with the spectral energy transfer is considered in § 5. We conclude with an interpretation and discussion of these findings in § 6.

2. Simulation details

We have conducted a set of DNS of 3D rotating RB in a horizontally periodic Cartesian computational box. By using a second-order energy-conserving, finite-difference code with fractional time stepping (Verzicco & Orlandi 1996), we march in time the Navier–Stokes equations plus an advection–diffusion equation for temperature, with the usual Boussinesq approximations (Chandrasekhar 1961):

$$\frac{\partial \boldsymbol{u}}{\partial t} + (\boldsymbol{u}\cdot\boldsymbol{\nabla})\boldsymbol{u} + \frac{1}{Ro}\boldsymbol{e}_z \times \boldsymbol{u} = -\boldsymbol{\nabla} p + \sqrt{\frac{Pr}{Ra}}\nabla^2\boldsymbol{u} + \theta \boldsymbol{e}_z, \tag{2.1}$$

$$\frac{\partial \theta}{\partial t} + (\boldsymbol{u}\cdot\boldsymbol{\nabla})\theta = \frac{1}{\sqrt{Ra\,Pr}}\nabla^2\theta, \tag{2.2}$$

with the incompressibility constraint

$$\boldsymbol{\nabla}\cdot\boldsymbol{u} = 0. \tag{2.3}$$

Here $\boldsymbol{u}$ is the velocity vector; t is time; $\boldsymbol{e}_z$ is the unit vector in the vertical direction; Ra is the Rayleigh number, i.e. the non-dimensional temperature difference, defined as $Ra = g\beta\Delta L^3/(\nu\kappa)$, with L the height of the system, β the thermal expansion coefficient of the fluid, g the gravitational acceleration, Δ the temperature difference between the bottom and top plates, and ν and κ the kinematic viscosity and thermal diffusivity of the fluid, respectively; Ro is the Rossby number, i.e. the inverse rotation rate, defined as $Ro = \sqrt{(\beta g\Delta/L)}/(2\Omega)$, with Ω the angular rotation rate; Pr is the Prandtl number of the fluid, $Pr = \nu/\kappa$; and θ is the non-dimensional temperature. Equations (2.1)–(2.3) are non-dimensionalised by using L, Δ and the so-called free-fall velocity scale $U = \sqrt{\beta g\Delta L}$. Note that centrifugal buoyancy is neglected here; this means that we are implicitly making the customary assumption that the Froude number $Fr = \Omega^2 R/g \ll 1$ (Stevens *et al.* 2013*a*), where R is the horizontal distance to the rotation axis, i.e. the radius of the cylinder in most experiments and simulations. We also define the Nusselt number, i.e. the non-dimensional heat transfer, as $Nu = (\langle u_z\theta\rangle_{A,t} - \kappa\partial\langle\theta\rangle_{A,t})/(\kappa\Delta L^{-1})$, with $\langle\cdots\rangle_{A,t}$ representing the averaging operator in time and also spatially over a horizontal plane.

Ra	Ek	Ro	$\widetilde{Ra}$	Γ	$N_x \times N_y \times N_z$	Nu_{SF}	Nu_{NS}	$N(\delta_v)$
1×10^{10}	4.00×10^{-7}	0.040	29.5	0.36	$384 \times 384 \times 768$	8.82	21.0	12
1×10^{10}	4.00×10^{-7}	0.040	29.5	0.71	$768 \times 768 \times 768$	9.13	21.0	12
1×10^{10}	6.00×10^{-7}	0.060	50.6	0.41	$384 \times 384 \times 768$	20.7	31.4	15
1×10^{10}	9.00×10^{-7}	0.090	86.9	0.46	$384 \times 384 \times 768$	46.2	50.2	17
1×10^{10}	1.20×10^{-6}	0.12	127.5	0.51	$384 \times 384 \times 768$	68.5	65.2	18
1×10^{10}	1.50×10^{-6}	0.15	171.7	0.55	$384 \times 384 \times 768$	91.0	76.0	20
1×10^{10}	2.00×10^{-6}	0.20	252.0	0.61	$512 \times 512 \times 768$	113.7	83.5	23
5×10^{10}	1.34×10^{-7}	0.030	34.3	0.25	$512 \times 512 \times 1024$	9.20	21.1	12
5×10^{10}	1.79×10^{-7}	0.040	50.4	0.27	$512 \times 512 \times 1024$	18.2	30.8	14
5×10^{10}	2.95×10^{-7}	0.066	98.3	0.32	$512 \times 512 \times 1024$	52.9	61.5	17
5×10^{10}	4.02×10^{-7}	0.090	148.6	0.36	$512 \times 512 \times 1024$	95.0	88.3	19
5×10^{10}	4.92×10^{-7}	0.11	194.2	0.38	$512 \times 512 \times 1024$	117.0	103.5	21
5×10^{10}	6.71×10^{-7}	0.15	293.6	0.42	$512 \times 512 \times 1024$	159.6	119.5	23

TABLE 1. Parameter values for the computations. For all runs, $Pr = 1$. Each parameter set has been run with both NS and SF boundary conditions. Included are: Rayleigh number Ra, Ekman number Ek, Rossby number Ro, $\widetilde{Ra} = Ra\,Ek^{4/3}$ (Sprague *et al.* 2006), domain aspect ratio $\Gamma = D/L$ (ratio of horizontal periodicity length D to domain height L) and number of grid points $N_x \times N_y \times N_z$ in the periodic directions and the vertical direction, respectively. We also list the resulting Nusselt numbers Nu_{SF} and Nu_{NS}, as well as the number of grid points $N(\delta_v)$ within the kinetic boundary layer in the NS runs (see also § 4.1). Typical time step sizes are 0.004 and 0.002 for $Ra = 1 \times 10^{10}$ and 5×10^{10}, respectively, expressed in convective time units H/U.

The explored parameter values are given in table 1. We vary the rotation rate Ro at a constant thermal driving Ra for two values of Ra, while fixing the Prandtl number to $Pr = 1$. The Ekman number, defined as $Ek = \nu/(2\Omega L^2) = Ro\sqrt{Pr/Ra}$, is small enough to enter into the geostrophic regime, as can be seen from table 1. For completeness, we also define the Taylor number $Ta = Ek^{-2}$. The aspect ratio, $\Gamma = D/L$, where D is the simulation box periodicity length in the horizontal directions, is set to 10 times the most unstable wavelength for convective instability, L_c, i.e. $\Gamma = 10L_c$. Wavelength L_c scales asymptotically as $L_c = 4.82Ek^{1/3}$, with minor corrections at finite Ek (Chandrasekhar 1961; Niiler & Bisshopp 1965; Heard & Veronis 1971). Here, we just take $\Gamma = 48.2Ek^{1/3}$. The boundary conditions for temperature are fixed as $\theta = 1$ at the bottom plate and $\theta = 0$ at the top plate. For velocity, we employ both no-slip (NS) boundary conditions, i.e. $\boldsymbol{u} = \boldsymbol{0}$ at both plates, and stress-free (SF) boundary conditions, i.e. $\partial_z u_x = \partial_z u_y = 0$ and $u_z = 0$ at the plates.

The grid is uniformly discretised in the horizontal direction. In the vertical direction, a clipped Chebyshev distribution is used to cluster points near the boundary layers. While the resulting boundary-layer thicknesses will be presented in § 4.1, we comment here on the adequacy of the near-wall resolution. The number of grid points found within the kinetic boundary layer is reported in the last column of table 1. The most demanding simulation at $Ra = 5 \times 10^{10}$ and $Ek = 1.34 \times 10^{-7}$ has 12 grid points within the kinetic boundary layer; the same is true for the case $Ra = 1 \times 10^{10}$ and $Ek = 4.00 \times 10^{-7}$. Higher Ekman numbers result in larger boundary-layer thicknesses and thus they are better resolved. The grid resolutions used here are in line with recent computations by Stellmach *et al.* (2014), and thus we consider them to be adequate.

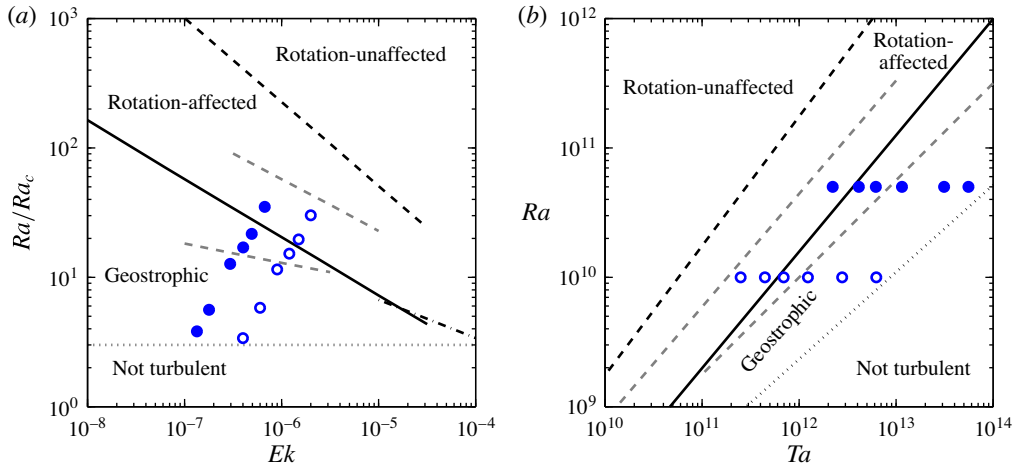

FIGURE 1. (Colour online) Phase diagram of rotating convection (*a*) in the $(Ek, Ra/Ra_c)$ parameter space, as suggested by Ecke & Niemela (2014), and (*b*) in the (Ta, Ra) parameter space (Vorobieff & Ecke 2002). The blue circles indicate the parameter values for which we have performed simulations using both no-slip (NS) and stress-free (SF) boundary conditions. The circles are either open for $Ra = 1 \times 10^{10}$ or filled for $Ra = 5 \times 10^{10}$. Three different regimes of convection can be discerned: non-rotating convection, rotation-affected convection and (rotation-dominated) geostrophic convection. The lines display various relations suggested in the literature that bound the regimes. Ecke & Niemela (2014) suggested $Ra/Ra_c = 3$ as a lower bound of the geostrophic regime (dotted black line), $Ra = 0.25Ek^{-1.8}$ for the transition between the geostrophic and rotation-affected regimes (solid black line), and $Ro = 0.35$ for the transition to the non-rotating regime (dashed black line). The dash-dotted black line is a transition valid for higher $Pr \approx 6$ (Ecke & Niemela 2014). Two alternative predictions for the transition to the geostrophic regime are also displayed: upper grey dashed line, $Ra = 1.4Ek^{-7/4}$ (King *et al.* 2009); and lower grey dashed line, $Ra \approx 10Ek^{-3/2}$ (King, Stellmach & Aurnou 2012).

For statistical convergence, the simulations are run until the temperature gradient at both plates is equal to less than 1 %, and the temporal convergence error of the Nusselt number measured through a volume average is smaller than 2 %. In practice, this means running the simulations between 100 and 200 convective time units, which are defined using the system height L and the free-fall velocity U. The total time varies: the lower Ek, the slower the convergence of statistics.

We tested the dependence on Γ of the simulations by running two cases at $Ra = 1 \times 10^{10}$ and $Ro = 0.04$ with a twice larger Γ (thus increasing the computational box size by a factor four, and hence the computational load by at least that amount). The Nusselt number is the same for no-slip plates but shows some difference in the stress-free case. For no-slip plates, we do not expect a strong dependence on Γ as long as it is large enough. However, for stress-free plates, differences may occur that are related to the flow structure. This will be addressed in more detail in § 5.

To indicate how the current simulations fit in with the previous work on this topic, we display our current parameter values in the $(Ek, Ra/Ra_c)$ phase diagram of figure 1, where Ra_c is the critical Rayleigh number for the onset of the convective instability with rotation, i.e. $Ra_c = 8.7Ek^{-4/3}$ (Chandrasekhar 1961), and in the (Ta, Ra) phase diagram. Figure 1(*a*) is based on figure 4 of Ecke & Niemela (2014), and shows

how the parameter values of the simulations in this paper are positioned relative to some of the proposed bounds on the geostrophic regime. Typically, a lower bound for the geostrophic regime is chosen such that the resulting flow is supercritical enough for a turbulent flow to develop. We follow Ecke & Niemela (2014) by choosing $Ra/Ra_c = 3$ (dotted black line in figure 1). Ecke & Niemela (2014) discern two additional transitions based on their heat-transfer measurements in cryogenic helium with $Pr = 0.7$. When reducing the Rayleigh number at constant Ek, the first transition seen is when rotation starts to reduce the heat transfer. This is well described by $Ro = 0.35$ (dashed black line in figure 1). When Ra is reduced even further, a transition to a steeper scaling law relating Nu and Ra was found. Ecke & Niemela (2014) interpreted this as the transition to the geostrophic regime. This transition was best described by the relation $Ra = 0.25Ek^{-1.8}$ (solid black line in figure 1) according to their data. For completeness, two other suggested relations for the transfer to the geostrophic regime have also been included in figure 1: $Ra = 1.4Ek^{-7/4}$ as suggested by King *et al.* (2009) (upper grey dashed line) and $Ra \approx 10Ek^{-3/2}$ from King *et al.* (2012) (lower grey dashed line). From the diagram, we expect our simulations to show a transition from the rotation-affected to the geostrophic regime for all criteria, except the one suggested by King *et al.* (2009).

3. Heat transfer

In this section, we investigate the convective heat transfer through the fluid layer as a function of the applied control parameters. In the geostrophic regime, no consensus has been reached on the heat-transfer dependence $Nu(Ra, Pr, Ek)$, in particular because it is challenging to achieve the extreme parameter values for Ra and Ek in both experiments and simulations. We summarise the results from the literature reported earlier in table 2, and indicate the method (experimental, numerical or from theory) and range of parameters considered. It must be emphasised that most of these works are outside of the geostrophic regime; the exceptions are the theories by King *et al.* (2012) and Julien *et al.* (2012*a*), as well as the numerical simulations by the latter authors, which consider the asymptotically reduced equations for rapid rotation.

The two recent experimental investigations that enter into the geostrophic regime show quite different results. Ecke & Niemela (2014) achieved $4 \times 10^9 < Ra < 4 \times 10^{11}$ and $2 \times 10^{-7} < Ek < 3 \times 10^{-5}$ at $Pr = 0.7$ used cryogenic helium gas as the working fluid. Their data could be described as $Nu \sim (Ra/Ra_c)^\gamma$, with $\gamma \approx 1$ using direct measurement or $1.2 < \gamma < 1.6$ after rescaling of the original data following existing theoretical arguments. The scaling ranges were not extensive enough to decisively discern between these scalings. On the other hand, Cheng *et al.* (2015) employed water as the working fluid. In their tall, slender cell, they could achieve $1 \times 10^{10} < Ra < 1 \times 10^{13}$ and $2 \times 10^{-8} < Ek < 2 \times 10^{-6}$ for $3.5 < Pr < 6.5$. They also reported scaling as $Nu \sim (Ra/Ra_c)^\gamma$, with a monotonically increasing γ from 1.8 at $Ek = 10^{-3}$ to 3.6 at $Ek = 10^{-7}$, based on a combination of experimental and DNS results.

Figure 2 shows Nu as a function of Ek obtained from the present simulations. By simple observation, it is clear that the boundary conditions (NS or SF) play a decisive role, even in the slope of the graph, i.e. the exponent α of the local scaling law $Nu \sim Ek^\alpha$. Both NS and SF boundary conditions display a transition in the scaling law (indicated with arrows in the graph) at $Ek \approx 9 \times 10^{-7}$ for $Ra = 1 \times 10^{10}$ and at $Ek \approx 3 \times 10^{-7}$ for $Ra = 5 \times 10^{10}$, as evidenced by the slope change. This transition is generally considered the boundary between rotation-affected and rotation-dominated convection (Ecke & Niemela 2014). At Ekman numbers below the transition, we observe distinctly different scalings with Ek. The SF exponents ($\alpha = 2.04$ for

https://doi.org/10.1017/jfm.2016.394 Published online by Cambridge University Press

Authors	Method	Scaling	Parameter range	Remark
King *et al.* (2009)	Exp. and num.	$Nu \sim Ra^{6/5}Ek^{8/5}$	$Ra < 6 \times 10^9;\ 1 \times 10^{-6} \leqslant Ek;\ 1 \leqslant Pr \leqslant 100$	NS
King *et al.* (2009) (supplement)	Num.	$Nu \sim Ra^{6/5}Ek^{8/5}$	$Ra < 6 \times 10^9;\ 1 \times 10^{-6} \leqslant Ek;\ 1 \leqslant Pr \leqslant 100$	SF
Schmitz & Tilgner (2009)	Num.	$Nu \sim Ra^{5/4}Ek^{3/2}$	$Ra \leqslant 2 \times 10^8;\ Ek \geqslant 1 \times 10^{-5}$ for $Pr = 0.7$	SF
			$Ra \leqslant 1 \times 10^8;\ Ek \geqslant 1 \times 10^{-5}$ for $Pr = 7$	SF
Schmitz & Tilgner (2010)	Num.	$Nu \sim Ra^{5/4}Ek^{3/2}$	$Ra \leqslant 1 \times 10^7;\ Ek \geqslant 1 \times 10^{-4};\ Pr = 7$	NS
King *et al.* (2012)	Theor.	$Nu \sim Ra^3Ek^4$	$Ra \lesssim Ek^{-3/2}$	—
Julien *et al.* (2012*a*)	Theor.	$Nu - 1 \sim Ra^{3/2}Ek^2$	—	—
	Num.	—	$0.3 \leqslant Pr \leqslant 1$ for $Ra\,Ek^{4/3} \gtrsim 80$	Asymptotic equations

TABLE 2. Proposed and observed scaling laws for the heat transfer in rotation-dominated convection found in the literature, expressed as $Nu(Ra, Ek)$. The Prandtl number dependence has been omitted, as it is out of the scope for the present paper. We also mention the range of parameters for which the scalings are intended or observed, as well as the method by which the scalings have been obtained ('exp.' for experiments, 'num.' for numerical simulations and 'theor.' for scaling arguments). Finally, the boundary conditions for the numerical studies are mentioned. These are the topic of the current work. The simulations by Julien *et al.* (2012*a*) are based on the asymptotic equations and employ what amounts to stress-free boundary conditions. Note that Schmitz & Tilgner (2009, 2010) have defined the Ekman number without the factor 2, hence the different parameter values in this table compared to their papers.

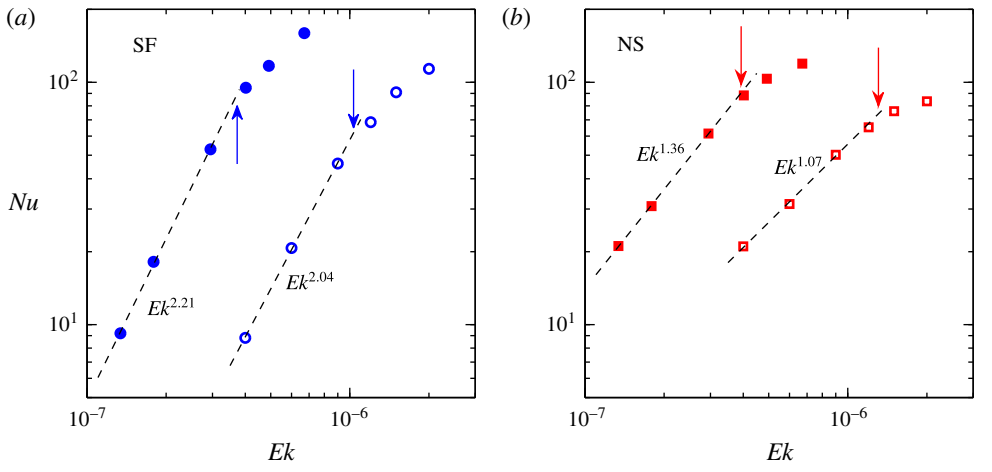

FIGURE 2. (Colour online) Heat transfer (Nusselt number Nu) as a function of the Ekman number Ek: (*a*) SF plates; (*b*) NS plates. Open symbols are for $Ra = 1 \times 10^{10}$; filled symbols for $Ra = 5 \times 10^{10}$. The dashed lines depict fitted power-law slopes. The arrows indicate the transition points as we inferred them from these graphs.

$Ra = 1 \times 10^{10}$ and $\alpha = 2.21$ for $Ra = 5 \times 10^{10}$) match fairly well (especially for the lower Ra case) with the theoretically predicted exponent $\alpha = 2$ of Julien *et al.* (2012*a*), found to be valid for simulations of the reduced equations, with boundary conditions that can be described as stress-free.

However, the NS runs reveal effective exponents $\alpha = 1.07$ for $Ra = 1 \times 10^{10}$ and $\alpha = 1.36$ for $Ra = 5 \times 10^{10}$, considerably lower than the SF runs and pronouncedly lower than the correlations inferred by King *et al.* (2012), which predict $\alpha = 4$ for NS plates. Schmitz & Tilgner (2009, 2010) have reported simulations with both NS and SF boundaries; they reported good agreement with the exponent 1.5, in fair agreement with the current NS runs (at least at $Ra = 5 \times 10^{10}$), but somewhat low for SF. The experiments by Ecke & Niemela (2014) have provided approximate scaling exponents between 1.6 and 2.1, depending on the exact plotting convention to attain data collapse.

It is worth noting that there is quite a difference in the applied Ra between the various works. Typically, values of Ra up to 5×10^9 are applied in experiments and simulations (King *et al.* 2009; Schmitz & Tilgner 2009, 2010; King *et al.* 2012; King, Stellmach & Buffett 2013), while only recently higher values have been attained – cf. simulations by Stellmach *et al.* (2014), experiments by Ecke & Niemela (2014) and Cheng *et al.* (2015), as well as the current simulations. It is plausible that what we observe is a new scaling regime opening up at such high Ra, strongly affected by rapid rotation (very low $Ek \sim O(10^{-7})$) but still vigorously turbulent (highly supercritical, i.e. $Ra/Ra_c \gg 1$), i.e. the geostrophic regime.

To further quantify the scaling laws, we show in figure 3 the compensated Nusselt number with the two scaling laws proposed by both King *et al.* (2012) and Julien *et al.* (2012*a*). Again, we can see that the $Nu \sim Ek^2$ (Julien *et al.* 2012*a*) captures well the Ekman-number dependence of the free-slip simulations below the transition, but the no-slip simulations present a very different dependence. The $Nu \sim Ek^4$ scaling law (King *et al.* 2012) can be seen to be a clear overestimate of the scaling exponent relating Nu and Ek.

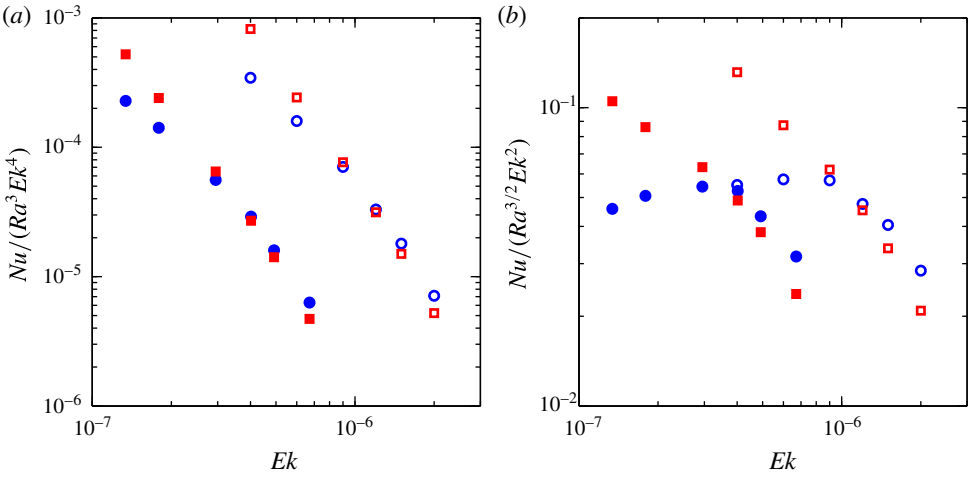

FIGURE 3. (Colour online) Compensated heat transfer (Nusselt number Nu) as a function of the Ekman number Ek using the proposed scaling laws: (*a*) $Nu \sim Ra^3Ek^4$ (King *et al.* 2012) and (*b*) $Nu \sim Ra^{3/2}Ek^2$ (Julien *et al.* 2012*a*). Open symbols are for $Ra = 1 \times 10^{10}$; filled symbols for $Ra = 5 \times 10^{10}$. The red squares represent no-slip boundary conditions, and blue circles free-slip boundary conditions.

Another striking feature of this graph is that, at the same Ra, there is a range for which Nu is lower for SF than for NS boundaries (Stellmach *et al.* 2014). Generally, NS boundaries are expected to reduce the turbulence intensity of the flow by introducing more friction than SF plates. However, the active nature of the Ekman boundaries, present for NS but absent for SF, can affect the dynamics of the entire fluid layer, enhancing the heat transfer instead of reducing it. We will revisit these results in later sections, where further differences between NS and SF runs are revealed and interpreted.

4. Boundary-layer and bulk dissipation

For RB convection, one can derive from the Navier–Stokes equations with the Boussinesq approximation exact relations for the total dissipation of turbulent kinetic energy and thermal variance within the domain (Shraiman & Siggia 1990). The energy equations are obtained by taking the inner product of $\boldsymbol{u}$ with (2.1) and multiplying (2.2) with θ, respectively. After applying the boundary conditions, the dissipation relations in dimensional form read

$$\epsilon_u = \frac{\nu^3}{L^4}(Nu - 1)Ra\,Pr^{-2}, \quad \epsilon_\theta = \kappa\frac{\Delta^2}{L^2}Nu, \tag{4.1a,b}$$

where ϵ_u is the (time- and volume-averaged) total dissipation of turbulent kinetic energy in the fluid layer and ϵ_θ is the total dissipation of thermal variance in the layer. These relations do not change when rotation is added: rotation only enters in the momentum equation (2.1), where we find for the Coriolis term in the energy equation that $\boldsymbol{u} \cdot (\boldsymbol{e}_z \times \boldsymbol{u}) = 0$.

The Grossmann–Lohse heat-transfer theory for non-rotating convection (see Ahlers, Grossmann & Lohse (2009) for an overview) is based on a division of the total dissipations into bulk and boundary-layer (BL) contributions. Several scaling regimes

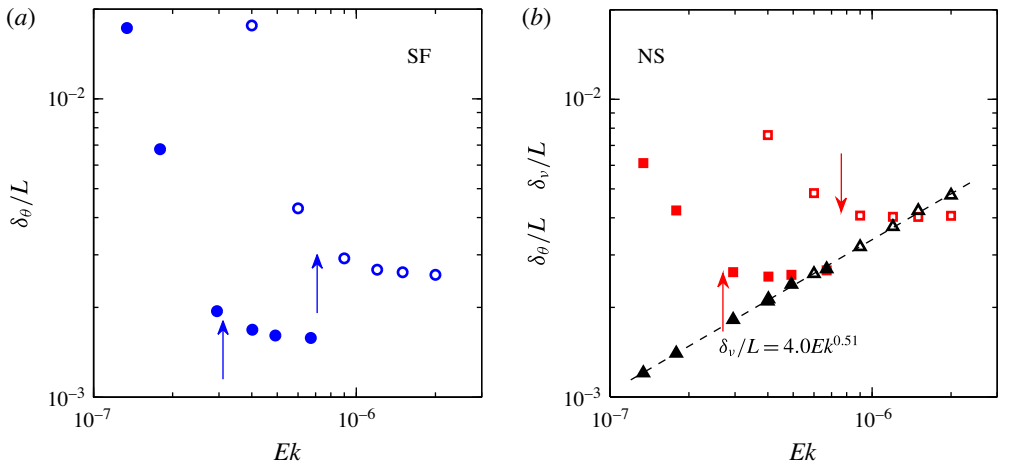

FIGURE 4. (Colour online) Boundary-layer thicknesses and their dependence on Ek: (*a*) SF plates, thermal BL thickness (δ_θ); (*b*) NS plates, thermal BL thickness (δ_θ, red squares) and kinetic BL thickness (δ_v, black triangles). The arrows indicate the transition points as inferred from these graphs, when the steeply decreasing δ_θ begins to flatten out. A power-law fit $\delta_v/L = 4.0Ek^{0.51}$ is also included (black dashed line). In both panels, open symbols are for $Ra = 1 \times 10^{10}$, and filled symbols for $Ra = 5 \times 10^{10}$.

can be found depending on the dominance of dissipation in either bulk or BL regions, for both ϵ_u and ϵ_θ. The theoretical arguments by Julien *et al.* (2012*a*) employ such a division for ϵ_θ (no division of ϵ_u given that in their SF case no kinetic BLs are formed) and show that the bulk limits the overall heat transfer in the geostrophic-turbulence state of the rotation-dominated geostrophic regime.

4.1. *Boundary-layer scales*

In this section we want to compare the distribution of dissipation for both NS and SF plates. To this end, we first need to discern between BL and bulk. Several BL scales have already been introduced in the RB literature. The thickness of the thermal BLs in the non-rotating case is well described by assuming that the bulk is isothermal, and that the temperature drop is fully accommodated by the BLs. This leads to the definition $\delta_{\theta,Nu}/L = 1/(2Nu)$. This relation is not appropriate for rotating RB convection, given that a mean temperature drop across the bulk is sustained (Julien *et al.* 1996). We therefore rely on the common definition of BL thicknesses in turbulence that uses the position of the peak value of the root mean square of temperature fluctuations, denoted by δ_θ. Julien *et al.* (2012*b*) found this definition to be the most appropriate one. For the kinetic (velocity) BLs we use the positions of the peak root mean square of horizontal velocities, marked δ_v.

A comparison of these BL scales is presented in figure 4. Starting from the kinetic BLs (black symbols), it is clear that they follow a single scaling, independent of Ra, i.e. their thickness is exclusively determined by Ek. A power law yields the relation $\delta_v/L = 4.0Ek^{0.51}$. Within error, the slope is consistent with the prediction $\delta_v \sim Ek^{1/2}$ for linear Ekman BLs (Greenspan 1968). It is worth noting that this scaling also matches nicely with the BL scaling laws reported by Kunnen *et al.* (2010*b*), even though the geometry (cylinder instead of periodic cube) and the Prandtl number ($Pr = 6.4$ instead of $Pr = 1$) are completely different.

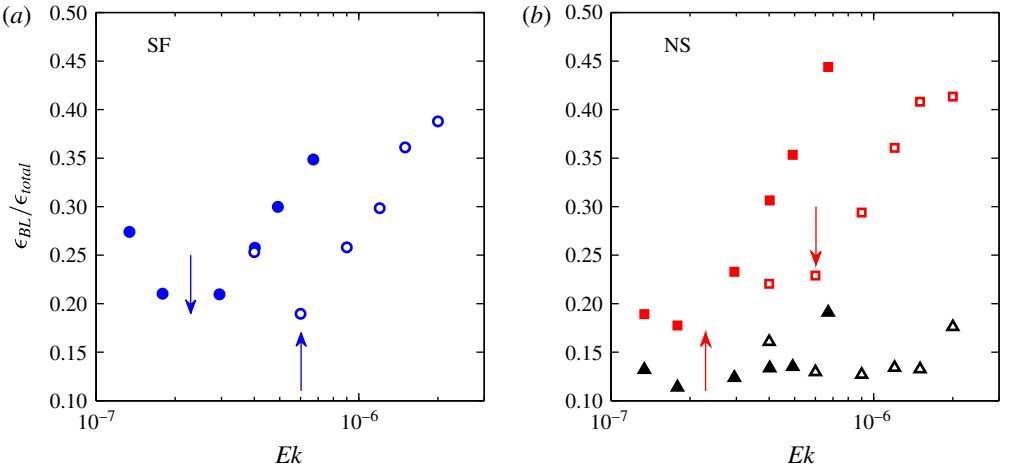

FIGURE 5. (Colour online) Distribution of dissipations ϵ_θ and ϵ_u between bulk and BL: (*a*) SF plates, ϵ_θ; (*b*) NS plates, ϵ_θ (red squares) and ϵ_u (black triangles). The fraction of total dissipation located in the BL region is displayed. Open symbols are for $Ra = 1 \times 10^{10}$; filled symbols for $Ra = 5 \times 10^{10}$. The arrows indicate the transition points as we inferred them from these graphs.

On the other hand, the thermal BL thicknesses do reveal some variation with Ek. Before the transition, the thermal BL thickness steeply decreases when Ek is increased, in contrast to the kinetic BLs. In that Ek range, the local scaling laws relating Nu and Ek are steeper for SF than for NS. King *et al.* (2009) and King *et al.* (2012) proposed that the transition to the rotation-dominated heat-flux scaling is described by the crossing of the kinetic and thermal BL thicknesses, which happens around $Ek = 7 \times 10^{-7}$ for NS and $Ra = 5 \times 10^{10}$ in this case. However, the slope change in the scaling laws (figure 2) is found at lower values of Ek. For $Ra = 1 \times 10^{10}$ a similar mismatch is observed.

A more natural definition of the transition, based on the BL scales as plotted in figure 4, would be the evident slope change of δ_θ at $Ek = 8 \times 10^{-7}$ for $Ra = 1 \times 10^{10}$ and at $Ek = 3 \times 10^{-7}$ for $Ra = 5 \times 10^{10}$, which remarkably occurs around the same Ek value for both NS and SF. This transition value matches better with the slope change in the heat-transfer statistics, even if they do not exactly coincide. The transition to the geostrophic regime thus appears to be gradual; different statistics display a change in behaviour at different values of Ek.

4.2. *Distribution of dissipation*

Using the BL scales of § 4.1, we can now assess how the total dissipation is distributed between BL and bulk regions. This is shown in figure 5, which confirms the picture that, under rapid rotation, the dissipation is mostly concentrated in the bulk. This is the case even more for ϵ_u than for ϵ_θ. However, we also note that the fraction of ϵ_θ in the BLs appears to start growing when Ek is reduced below $\sim 5 \times 10^{-7}$ ($\sim 2 \times 10^{-7}$) for $Ra = 1 \times 10^{10}$ (5×10^{10}), with an earlier growth appearing for SF than for NS. Looking back to figure 4, it is obvious that the thermal BLs are expanding when Ek is reduced. The larger part of the volume inside the thermal BLs along with a persistent input of thermal fluctuations from the Ekman BLs enhances

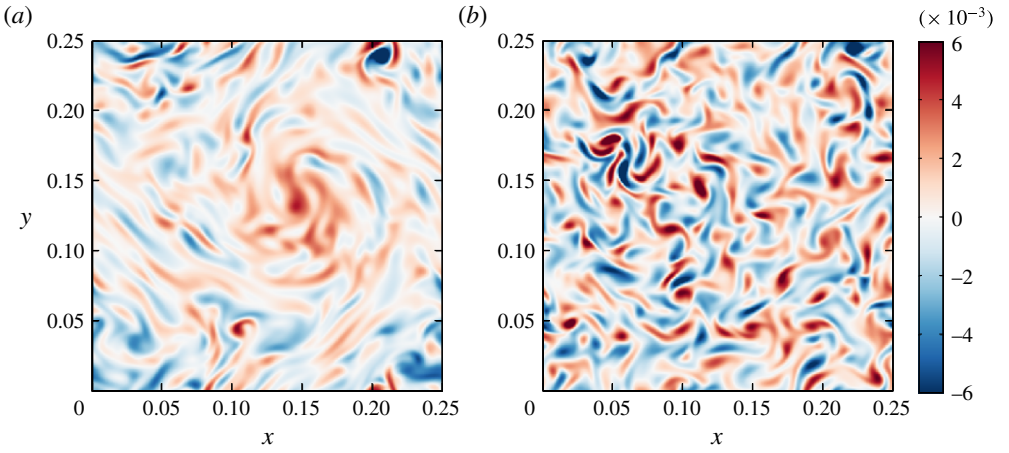

FIGURE 6. (Colour online) Snapshot at mid-height ($z = 0.5$) of the vertical vorticity from runs at $Ra = 5 \times 10^{10}$ and $Ek = 1.34 \times 10^{-7}$: (*a*) SF plates; (*b*) NS plates. Red is positive (cyclonic) vorticity, while blue is negative (anticyclonic) vorticity. Both plots have the same colour scale.

the BL fraction of ϵ_θ at the lowest considered Ek under NS conditions. For SF plates the thermal BLs are growing even more as Ek is reduced; the increased volume of the BLs appears to be enough for a higher fraction of ϵ_θ there.

Furthermore, the contribution of the kinetic BLs to the total ϵ_u is remarkable: for $Ra = 5 \times 10^{10}$, between $Ek = 1.3 \times 10^{-7}$ and $Ek = 5 \times 10^{-7}$ the BL thickness changes by a factor 2, yet the fraction of ϵ_u in the BL remains roughly constant. This confirms that the Ekman BLs, first thought to become passive at low enough Ek (Niiler & Bisshopp 1965; Heard & Veronis 1971; Julien & Knobloch 1998), are still significantly affecting the flow dynamics (Stellmach *et al.* 2014).

5. Flow phenomenology

A remarkable phenomenological change upon entering the geostrophic-turbulence state of the rotation-dominated geostrophic regime is the disappearance of convective Taylor columns and plumes as a result of a loss of vertical coherence (Sprague *et al.* 2006; Julien *et al.* 2012*b*; Stellmach *et al.* 2014). These vortical structures have been frequently reported ever since the first observation in turbulent rotating RB flow by Rossby (1969). In the geostrophic-turbulence state, however, such coherent structures seem to be absent. The boundary conditions largely determine the flow phenomenology. For SF plates, large barotropic vortices can be formed under the influence of an inverse energy cascade (Favier *et al.* 2014; Guervilly *et al.* 2014; Rubio *et al.* 2014; Stellmach *et al.* 2014), eventually growing to the scale of the domain. For NS plates, such a condensate is not formed. We compare the phenomenology in two snapshots shown in figure 6, which depict the spatial distribution of vertical vorticity $\omega_z = \partial_x u_y - \partial_y u_x$ in a horizontal cross-section at mid-height. Figure 6(*a*) clearly reveals the formation of a large cyclonic vortex in the top right, while the bottom-right part and its periodic continuation on opposite sides hint at the formation of an anticyclonic vortex. Note that this flow is still slowly evolving over time (Favier *et al.* 2014; Guervilly *et al.* 2014; Rubio *et al.* 2014).

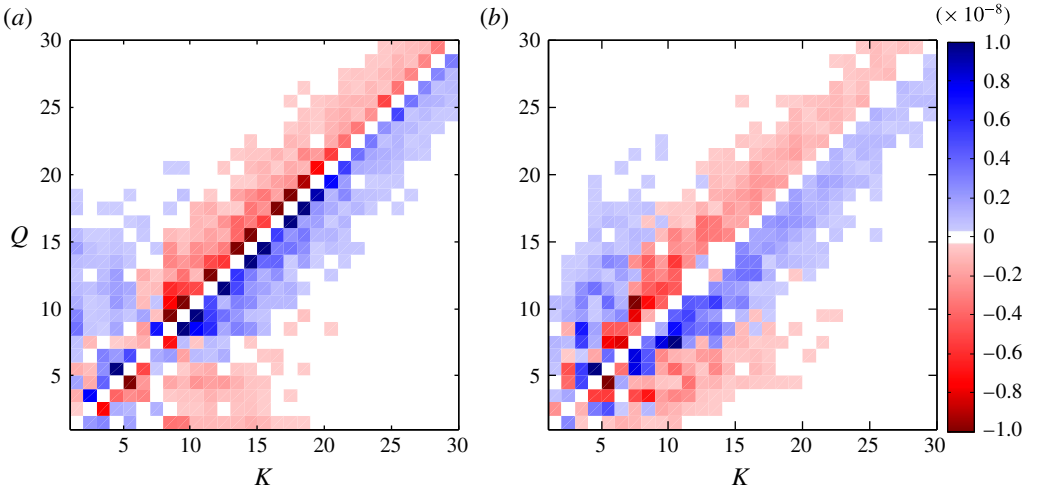

FIGURE 7. (Colour online) Spectral energy transfer $T(Q, K)$ between wavenumber shells Q and K: (*a*) for SF and (*b*) for NS. Positive values indicate that energy is taken from shell Q and transferred to shell K; negative values imply that Q receives energy from K. Both plots have the same colour scale.

Figure 6(*b*) shows no condensate vortices. Instead, a fluctuating state is found without large-scale long-lived coherent structure. Ekman pumping, present only in the case of NS boundary conditions, can thus be a source of small-scale fluctuations that prevent condensation into large-scale vortices.

5.1. *Relation with spectral energy transfer*

In previous works (Favier *et al.* 2014; Rubio *et al.* 2014), the energy transfer as a function of wavenumber has been considered to indicate the presence of an inverse energy cascade. Given that figure 6 reveals such a significant difference in flow phenomenology between SF and NS, we anticipate that the spectral energy transfer must also be considerably different. Following Favier *et al.* (2014), we define the spectral energy equation as

$$\frac{\mathrm{d}E(K)}{\mathrm{d}t} = \sum_{Q} T(Q, K) - D(K) + F(K), \tag{5.1}$$

which gives the temporal evolution of the energy $E(K)$ as a function of horizontal wavenumber K in terms of the energy transfer $T(Q, K)$ from wavenumber shell Q to shell K, the dissipation $D(K)$ and the buoyant forcing $F(K)$. We are particularly interested in the transfer term $T(Q, K)$, which we evaluate and average vertically over the entire computational domain minus the BLs. We note that this quantity is antisymmetric by definition, i.e. $T(K_1, K_2) = -T(K_2, K_1)$ and $T(K_1, K_1) = 0$ for any two wavenumbers K_1 and K_2.

The spectral transfer at $Ra = 5 \times 10^{10}$ and $Ek = 1.34 \times 10^{-7}$ is depicted in figure 7, for both SF and NS conditions. We note that we are only showing the first 30 modes, of a total of 256 in the simulation, so the dispersive errors of finite-difference schemes are negligible in this range. The SF picture compares favourably to the

earlier studies by Favier *et al.* (2014) and Rubio *et al.* (2014): a strong localised exchange of energy between neighbouring wavenumbers across the diagonal, i.e. a certain mode P interacts predominantly with its neighbouring modes $P-1$ and $P+1$. The sign of the transfer reveals that this part of the cascade is direct: energy is transferred to larger wavenumbers. At low $K \lesssim 7$ and higher $Q \gtrsim 7$, a range of inverse transfer is found where small-K modes receive energy from modes $Q > K$. The input of energy into the large-scale vortex of figure 6(*a*) can be recognised as an interaction of the smallest wavenumbers receiving energy from a broad range of higher-order wavenumbers. Such a non-local inverse cascade has been observed before in rotating convection by Favier *et al.* (2014), who could display a clearer effect due to a considerably larger domain. It is also similar to the inverse energy cascade in rotating turbulence (Mininni, Alexakis & Pouquet 2009). The non-locality indicates that the largest flow scale directly receives energy from the smaller scales without passing through intermediate scales. In contrast, in the direct cascade, energy is transferred from large to small while passing through all intermediate scales.

For the NS case (figure 7*b*), the picture changes. In particular, the 'staircase' of energy transfer along the diagonal, which is prominent for SF, is not as strongly present for the larger wavenumbers. Instead, the interactions between modes are less localised, meaning that the interactions are spread more and mode combinations farther from the diagonal are transferring energy. A direct cascade is formed along the diagonal for $K, Q \gtrsim 5$. Curiously, some signs of an inverse cascade remain: (i) for $K \leqslant 5$, and (ii) transfers from modes around $Q \approx 5$ to $K \approx 10$, which are non-localised. The absence of a large-scale structure can be explained by the fact that the lowest wavenumber is receiving considerably less energy and from a narrower range of scales than in SF.

5.2. *Relation with mean temperature gradient*

The characteristic flow phenomenology of rotating RB convection has been related to the occurrence (and strength) of the persistent mean temperature gradient across the bulk (Julien *et al.* 1996), unlike the statistically isothermal bulk of non-rotating RB. The origin of this temperature gradient has been proposed to be increased by lateral mixing, induced by interactions of like-signed vortical plumes. As in the geostrophic-turbulence state the flow phenomenology is altered (cf. figure 6), we can expect that this also affects the strength of the mean temperature gradient. Figure 8 shows the mean temperature gradient as a function of Ek. In the rotation-affected RB, lateral mixing being stronger than vertical mixing leads to mean temperature gradients as large as -0.5 for NS and -0.4 for SF. However, upon entering the geostrophic-turbulence state by further reducing Ek, the magnitude of the gradient is gradually diminished. We thus expect that in the geostrophic-turbulence state the mixing can become slightly more 3D again.

This behaviour is consistent with previous simulations of the asymptotic equations (Julien *et al.* 2012*b*), which predict that the geostrophic-turbulence state indeed still has a mean temperature gradient, but less steep than when coherent vortical plumes are present. Finally, even though the behaviour of the mean temperature gradient is qualitatively similar for SF and NS plates, the location of the minimum temperature gradient, which could be taken as an additional indicator for the transition, certainly does not coincide between the two cases.

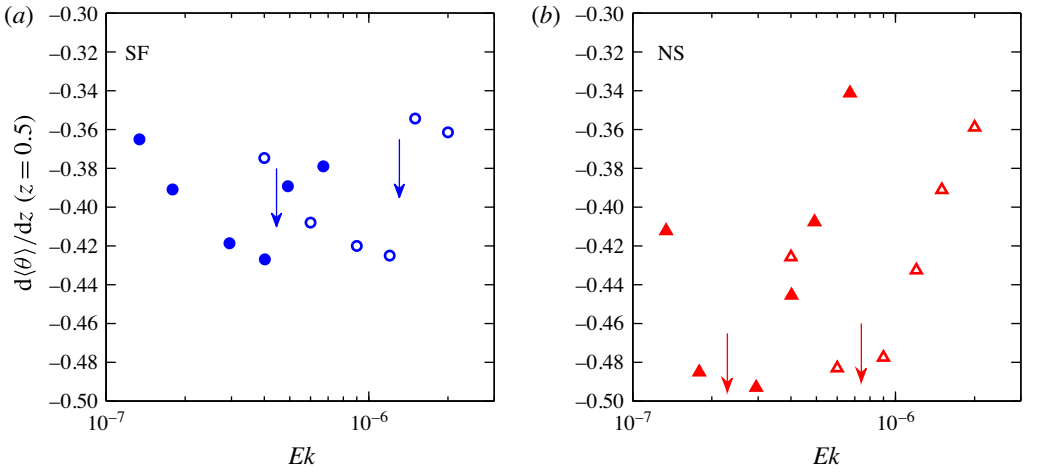

FIGURE 8. (Colour online) Mean temperature gradient at midplane: (*a*) for SF and (*b*) for NS. Open symbols are for $Ra = 1 \times 10^{10}$; filled symbols for $Ra = 5 \times 10^{10}$. The arrows indicate the transition points as inferred from these graphs.

6. Discussion

In the previous sections we have compared the transition to the geostrophic regime of turbulent rotating RB convection between SF and NS boundary conditions on the horizontal plates. From the current results, it seems clear that the nature of the bulk turbulence is extremely dependent on the boundary conditions. Nevertheless, both types of boundary conditions display a transition in a similar range of Ekman numbers around $Ek = 9 \times 10^{-7}$ (3×10^{-7}) for $Ra = 1 \times 10^{10}$ (5×10^{10}). This transition is found to be gradual, unlike other transitions in rotating RB flow, such as those reported in confined geometries at higher Ek (Stevens *et al.* 2009). Many diagnostic signs of flow transition can be found near the onset of the geostrophic regime: the scaling with Ek of many quantities including Nusselt number, thermal BL thickness, bulk–BL distribution of dissipation rates as well as the midplane mean temperature gradient show a changing behaviour. We do not expect this list to be exhaustive. All quantities show a transition centred at a specific Ek, so that the full range of changes covers at least half a decade in Ek. In particular, at $Ra = 1 \times 10^{10}$ we inferred transitions in various statistics in the range $6 \times 10^{-7} \lesssim Ek \lesssim 1.3 \times 10^{-6}$; at $Ra = 5 \times 10^{10}$ in the range $2.4 \times 10^{-7} \lesssim Ek \lesssim 4.5 \times 10^{10}$. These ranges are the same for SF and NS plates; however, individual statistics display transitions at different Ek when comparing the two boundary conditions. So it appears to be all but impossible to define a single criterion to distinguish the rotation-dominated geostrophic regime from the rotation-affected regime, as indeed the flow may be transitioning, but the different diagnostic quantities may be sensitive slightly before or slightly after the transition.

Regarding the actual nature of the transition, it is quite remarkable that the SF and NS transition ranges coincide in Ek for similar Ra. This would suggest a common origin. One of two candidates (or a combination of both) suggested in the literature may be the cause: either marginal (in)stability of the thermal BL, as suggested by King *et al.* (2012), which leads to a theoretical scaling $Nu \sim Ra^3 Ek^4$; or a change in the bulk dynamics where plumes cannot enter the stiff geostrophic bulk that

throttles the heat transport, suggested by Julien *et al.* (2012*a*), which gives a scaling $Nu \sim Ra^{3/2}Ek^2$. Both arguments could in principle be independent of the velocity boundary conditions, given that either the thermal BLs or the bulk flow away from the BLs is involved. We find mostly evidence supporting the Julien *et al.* (2012*a*) mechanism, but it is certainly not conclusive:

(i) The geostrophic Nusselt-number scaling of figure 2 matches fairly with the Julien *et al.* (2012*a*) scaling for SF plates, but not for NS. The scaling proposed by King *et al.* (2012) does not match with the current results for either boundary condition. In line with the recent experimental results of Cheng *et al.* (2015), it is becoming clear that the heat-transfer scaling exponent β for $Nu \sim Ra^{\beta}$ measured at constant Ek is not the same for all Ek; equivalently, the exponent γ for $Nu \sim Ek^{\gamma}$ at constant Ra will take different values for different Ra.

(ii) For the BL thickness (figure 4) we find a change in scaling at $Ek = 8 \times 10^{-7}$ (3×10^{-7}) at $Ra = 1 \times 10^{10}$ (5×10^{10}) for both SF and NS, with steeper scaling with Ek below the transition. The transition does not coincide with the crossing of the kinetic and thermal BL thicknesses, which is the criterion proposed by King *et al.* (2009, 2012) to describe its origin. The sharp change of scaling indicates changes in the structure of the thermal BL, which could be due to the crossing of the marginal stability criterion for the BL. However, the corresponding limit of validity $Ra \lesssim Ek^{-3/2}$ for the argument (King *et al.* 2012) would at the current $Ra = 5 \times 10^{10}$ predict a transition at $Ek \approx 7 \times 10^{-8}$, at significantly smaller Ek than we observe.

(iii) Finally, the spatial distribution of dissipation of both turbulent kinetic energy (ϵ_θ) and thermal variance (ϵ_u) between bulk and BL (figure 5) reveals that most of the dissipation is found to occur in the bulk, even more so for ϵ_u than for ϵ_θ. The fractional distribution between bulk and BL reveals a slope change at $Ek \approx 6 \times 10^{-7}$ (2×10^{-7}) at $Ra = 1 \times 10^{10}$ (5×10^{10}) for both SF and NS.

For SF plates, the Julien *et al.* (2012*a*) arguments fit best with our findings. However, the case of NS plates requires a different description given the presence of Ekman layers that are significantly affecting the flow dynamics in the entire fluid layer. We presently cannot give a theoretical description, but we expect that these results, together with the recent findings by Stellmach *et al.* (2014) and Cheng *et al.* (2015), can form a starting point for theories of no-slip geophysical convection. In that respect we want to mention here the recent work by Julien *et al.* (2016) where Ekman pumping is incorporated into the asymptotically reduced equations.

In conclusion, it has become apparent in the last few years that the Ekman layers remain a decisive and active part of geostrophic convection with no-slip plates, in spite of their diminishing thickness. We have compared the transition to the geostrophic regime between no-slip and stress-free boundaries. Both undergo a transition, at roughly the same Ekman number, but the scaling laws for heat transfer on both sides of the transition are strongly dependent on the boundary conditions. The physical picture of geostrophic convection is not fully complete, especially for no-slip plates.

Acknowledgements

We would like to thank S. Grossmann, C. Sun and Y. Yang for various stimulating discussions. We also thank the reviewers for their detailed and constructive comments, which have helped tremendously to improve the introductory paragraphs in particular. We acknowledge FOM, an ERC Advanced Grant, the PRACE resource Hermit based in Stuttgart at HLRS, and NWO for the use of Cartesius under grant no. SH-202.

REFERENCES

AHLERS, G., GROSSMANN, S. & LOHSE, D. 2009 Heat transfer and large scale dynamics in turbulent Rayleigh–Bénard convection. *Rev. Mod. Phys.* **81**, 503–537.

BASSOM, A. P. & ZHANG, K. 1994 Strongly nonlinear convection cells in a rapidly rotating fluid layer. *Geophys. Astrophys. Fluid Dyn.* **76**, 223–238.

CHANDRASEKHAR, S. 1961 *Hydrodynamic and Hydromagnetic Stability*. Oxford University Press.

CHENG, J. S., STELLMACH, S., RIBEIRO, A., GRANNAN, A., KING, E. M. & AURNOU, J. M. 2015 Laboratory-numerical models of rapidly rotating convection in planetary cores. *Geophys. J. Int.* **201**, 1–17.

CLUNE, T. & KNOBLOCH, E. 1993 Pattern selection in rotating convection with experimental boundary conditions. *Phys. Rev.* E **47**, 2536–2550.

DAWES, J. H. P. 2001 Rapidly rotating thermal convection at low Prandtl number. *J. Fluid Mech.* **428**, 61–80.

ECKE, R. E. 2015 Scaling of heat transport near onset in rapidly rotating convection. *Phys. Lett.* A **379**, 2221–2223.

ECKE, R. E. & NIEMELA, J. J. 2014 Heat transport in the geostrophic regime of rotating Rayleigh–Bénard convection. *Phys. Rev. Lett.* **113**, 114301.

FAVIER, B., SILVERS, L. J. & PROCTOR, M. R. E. 2014 Inverse cascade and symmetry breaking in rapidly rotating Boussinesq convection. *Phys. Fluids* **26**, 096605.

GREENSPAN, H. P. 1968 *The Theory of Rotating Fluids*. Cambridge University Press.

GROOMS, I., JULIEN, K., WEISS, J. B. & KNOBLOCH, E. 2010 Model of convective Taylor columns in rotating Rayleigh–Bénard convection. *Phys. Rev. Lett.* **104**, 224501.

GROSSMANN, S. & LOHSE, D. 2000 Scaling in thermal convection: a unifying theory. *J. Fluid Mech.* **407**, 27–56.

GROSSMANN, S. & LOHSE, D. 2001 Thermal convection for large Prandtl numbers. *Phys. Rev. Lett.* **86**, 3316–3319.

GROSSMANN, S. & LOHSE, D. 2004 Fluctuations in turbulent Rayleigh–Bénard convection: the role of plumes. *Phys. Fluids* **16**, 4462–4472.

GUERVILLY, C., HUGHES, D. W. & JONES, C. A. 2014 Large-scale vortices in rapidly rotating Rayleigh–Bénard convection. *J. Fluid Mech.* **758**, 407–435.

HEARD, W. B. & VERONIS, G. 1971 Asymptotic treatment of the stability of a rotating layer of fluid with rigid boundaries. *Geophys. Fluid Dyn.* **2**, 299–316.

HEIMPEL, M., AURNOU, J. & WICHT, J. 2005 Simulation of equatorial and high-latitude jets on Jupiter in a deep convection model. *Nature* **438**, 193–196.

HORN, S. & SHISHKINA, O. 2014 Toroidal and poloidal energy in rotating Rayleigh–Bénard convection. *J. Fluid Mech.* **762**, 232–255.

JULIEN, K., AURNOU, J. M., CALKINS, M. A., KNOBLOCH, E., MARTI, P., STELLMACH, S. & VASIL, G. M. 2016 A nonlinear model for rotationally constrained convection with Ekman pumping. *J. Fluid Mech.* **798**, 50–87.

JULIEN, K. & KNOBLOCH, E. 1998 Strongly nonlinear convection cells in a rapidly rotating fluid layer: the tilted f-plane. *J. Fluid Mech.* **360**, 141–178.

JULIEN, K., LEGG, S., MCWILLIAMS, J. & WERNE, J. 1996 Rapidly rotating turbulent Rayleigh–Bénard convection. *J. Fluid Mech.* **322**, 243–273.

JULIEN, K., KNOBLOCH, E., RUBIO, A. M. & VASIL, G. M. 2012*a* Heat transport in low-Rossby-number Rayleigh–Bénard convection. *Phys. Rev. Lett.* **109**, 254503.

JULIEN, K., RUBIO, A. M., GROOMS, I. & KNOBLOCH, E. 2012*b* Statistical and physical balances in low Rossby number Rayleigh–Bénard convection. *Geophys. Astrophys. Fluid Dyn.* **106**, 392–428.

KING, E. M. & AURNOU, J. M. 2012 Thermal evidence for Taylor columns in turbulent rotating Rayleigh–Bénard convection. *Phys. Rev.* E **85**, 016313.

KING, E. M., STELLMACH, S. & AURNOU, J. M. 2012 Heat transfer by rapidly rotating Rayleigh–Bénard convection. *J. Fluid Mech.* **691**, 568–582.

KING, E. M., STELLMACH, S. & BUFFETT, B. 2013 Scaling behaviour in Rayleigh–Bénard convection with and without rotation. *J. Fluid Mech.* **717**, 449–471.

KING, E. M., STELLMACH, S., NOIR, J., HANSEN, U. & AURNOU, J. M. 2009 Boundary layer control of rotating convection systems. *Nature* **457**, 301–304.

KUNNEN, R. P. J., CLERCX, H. J. H. & GEURTS, B. J. 2006 Heat flux intensification by vortical flow localization in rotating convection. *Phys. Rev.* E **74**, 056306.

KUNNEN, R. P. J., CLERCX, H. J. H. & GEURTS, B. J. 2008*a* Breakdown of large-scale circulation in turbulent rotating convection. *Europhys. Lett.* **84**, 24001.

KUNNEN, R. P. J., CLERCX, H. J. H. & GEURTS, B. J. 2008*b* Enhanced vertical inhomogeneity in turbulent rotating convection. *Phys. Rev. Lett.* **101**, 174501.

KUNNEN, R. P. J., CLERCX, H. J. H. & GEURTS, B. J. 2010*a* Vortex statistics in turbulent rotating convection. *Phys. Rev.* E **82**, 036306.

KUNNEN, R. P. J., GEURTS, B. J. & CLERCX, H. J. H. 2010*b* Experimental and numerical investigation of turbulent convection in a rotating cylinder. *J. Fluid Mech.* **642**, 445–476.

KUNNEN, R. P. J., CORRE, Y. & CLERCX, H. J. H. 2013 Vortex plume distribution in confined turbulent rotating convection. *Eur. Phys. Lett.* **104**, 54002.

KUNNEN, R. P. J., STEVENS, R. J. A. M., OVERKAMP, J., SUN, C., VAN HEIJST, G. J. F. & CLERCX, H. J. H. 2011 The role of Stewartson and Ekman layers in turbulent rotating Rayleigh–Bénard convection. *J. Fluid Mech.* **688**, 422–442.

LIU, Y. & ECKE, R. E. 1997 Heat transport scaling in turbulent Rayleigh–Bénard convection: effects of rotation and Prandtl number. *Phys. Rev. Lett.* **79**, 2257–2260.

LIU, Y. & ECKE, R. E. 2009 Heat transport measurements in turbulent rotating Rayleigh–Bénard convection. *Phys. Rev.* E **80**, 036314.

LIU, Y. & ECKE, R. E. 2011 Local temperature measurements in turbulent rotating Rayleigh–Bénard convection. *Phys. Rev.* E **84**, 016311.

MARSHALL, J. & SCHOTT, F. 1999 Open-ocean convection: observations, theory, and models. *Rev. Geophys.* **37**, 1–64.

MIESCH, M. S. 2000 The coupling of solar convection and rotation. *Solar Phys.* **192**, 59–89.

MININNI, P. D., ALEXAKIS, A. & POUQUET, A. 2009 Scale interactions and scaling laws in rotating flows at moderate Rossby numbers and large Reynolds numbers. *Phys. Fluids* **21**, 015108.

NAKAGAWA, Y. & FRENZEN, P. 1955 A theoretical and experimental study of cellular convection in rotating fluids. *Tellus* **7**, 1–21.

NIILER, P. P. & BISSHOPP, F. E. 1965 On the influence of Coriolis forces on onset of thermal convection. *J. Fluid Mech.* **22**, 753–761.

PORTEGIES, J. W., KUNNEN, R. P. J., VAN HEIJST, G. J. F. & MOLENAAR, J. 2008 A model for vortical plumes in rotating convection. *Phys. Fluids* **20**, 066602.

ROBERTS, P. & GLATZMAIER, G. 2000 Geodynamo theory and simulations. *Rev. Mod. Phys.* **72**, 1081–1123.

ROSSBY, H. T. 1969 A study of Bénard convection with and without rotation. *J. Fluid Mech.* **36**, 309–335.

RUBIO, A. M., JULIEN, K., KNOBLOCH, E. & WEISS, J. B. 2014 Upscale energy transfer in three-dimensional rapidly rotating turbulent convection. *Phys. Rev. Lett.* **112**, 144501.

SAKAI, S. 1997 The horizontal scale of rotating convection in the geostrophic regime. *J. Fluid Mech.* **333**, 85–95.

SCHMITZ, S. & TILGNER, A. 2009 Heat transport in rotating convection without Ekman layers. *Phys. Rev.* E **80**, 015305(R).

SCHMITZ, S. & TILGNER, A. 2010 Transitions in turbulent rotating Rayleigh–Bénard convection. *Geophys. Astrophys. Fluid Dyn.* **104**, 481–489.

SHRAIMAN, B. I. & SIGGIA, E. D. 1990 Heat transport in high-Rayleigh-number convection. *Phys. Rev.* A **42**, 3650–3653.

SPRAGUE, M., JULIEN, K., KNOBLOCH, E. & WERNE, J. 2006 Numerical simulation of an asymptotically reduced system for rotationally constrained convection. *J. Fluid Mech.* **551**, 141–174.

STELLMACH, S., LISCHPER, M., JULIEN, K., VASIL, G., CHENG, J. S., RIBEIRO, A., KING, E. M. & AURNOU, J. M. 2014 Approaching the asymptotic regime of rapidly rotating convection: boundary layers versus interior dynamics. *Phys. Rev. Lett.* **113**, 254501.

STEVENS, R. J. A. M., CLERCX, H. J. H. & LOHSE, D. 2010 Optimal Prandtl number for heat transfer in rotating Rayleigh–Bénard convection. *New J. Phys.* **12**, 075005.

STEVENS, R. J. A. M., CLERCX, H. J. H. & LOHSE, D. 2012 Breakdown of the large-scale circulation in $\Gamma = 1/2$ rotating Rayleigh–Bénard flow. *Phys. Rev.* E **86**, 056311.

STEVENS, R. J. A. M., CLERCX, H. J. H. & LOHSE, D. 2013*a* Heat transport and flow structure in rotating Rayleigh–Bénard convection. *Eur. J. Mech. (*B*/Fluids)* **40**, 41–49.

STEVENS, R. J. A. M., VAN DER POEL, E. P., GROSSMANN, S. & LOHSE, D. 2013*b* The unifying theory of scaling in thermal convection: the updated prefactors. *J. Fluid Mech.* **730**, 295–308.

STEVENS, R. J. A. M., ZHONG, J.-Q., CLERCX, H. J. H., AHLERS, G. & LOHSE, D. 2009 Transitions between turbulent states in rotating Rayleigh–Bénard convection. *Phys. Rev. Lett.* **103**, 024503.

VERONIS, G. 1968 Large-amplitude Bénard convection in a rotating fluid. *J. Fluid Mech.* **31**, 113–139.

VERZICCO, R. & ORLANDI, P. 1996 A finite-difference scheme for three-dimensional incompressible flow in cylindrical coordinates. *J. Comput. Phys.* **123**, 402–413.

VOROBIEFF, P. & ECKE, R. E. 2002 Turbulent rotating convection: an experimental study. *J. Fluid Mech.* **458**, 191–218.

WEISS, S. & AHLERS, G. 2011*a* Heat transport by turbulent rotating Rayleigh–Bénard convection and its dependence on the aspect ratio. *J. Fluid Mech.* **684**, 407–426.

WEISS, S. & AHLERS, G. 2011*b* The large-scale flow structure in turbulent rotating Rayleigh–Bénard convection. *J. Fluid Mech.* **688**, 461–492.

WEISS, S., STEVENS, R. J. A. M., ZHONG, J.-Q., CLERCX, H. J. H., LOHSE, D. & AHLERS, G. 2010 Finite-size effects lead to supercritical bifurcations in turbulent rotating Rayleigh–Bénard convection. *Phys. Rev. Lett.* **105**, 224501.

ZHONG, F., ECKE, R. E. & STEINBERG, V. 1993 Rotating Rayleigh–Bénard convection: asymmetric modes and vortex states. *J. Fluid Mech.* **249**, 135–159.

ZHONG, J.-Q. & AHLERS, G. 2010 Heat transport and the large-scale circulation in rotating turbulent Rayleigh–Bénard convection. *J. Fluid Mech.* **665**, 300–333.

ZHONG, J.-Q., STEVENS, R. J. A. M., CLERCX, H. J. H., VERZICCO, R., LOHSE, D. & AHLERS, G. 2009 Prandtl-, Rayleigh-, and Rossby-number dependence of heat transport in turbulent rotating Rayleigh–Bénard convection. *Phys. Rev. Lett.* **102**, 044502.